



Manufacturability and Mechanical Assessment of Ti-6Al-4V 3D Printed Structures for Patient-Specific Implants

Fatemeh Zarei¹ · Aziz Shafiei-Zarghani^{1,2,3} · Fatemeh Dehnavi¹

Received: 17 November 2022 / Accepted: 24 April 2023 / Published online: 25 May 2023
© The Author(s), under exclusive licence to Shiraz University 2023

Abstract

Recent advancements in additive manufacturing technology for metallic materials have paved the way for the creation of patient-specific implants with tailored mechanical properties for bone tissue reconstruction. To address the issue of stress shielding and improve osseointegration, the implants feature an architected internal structure with a unique design capable of mimicking the mechanical properties of the damaged bone. This study proposes a fast, simple, and clinically applicable approach for designing trabecular-like structures for tailored implants, specifically for the tibia component in knee joint replacement. The lattice structures with different solid fractions were designed and fabricated using the selective laser melting (SLM) technique and Ti-6Al-4V alloy. The mechanical behavior of the structures was evaluated through computational and experimental analysis, and compared with that of natural tibia bone. Moreover, the manufacturing robustness of the printed structures was assessed using X-ray computed tomography and microscopic examinations. Results show that the permeability of the fabricated structures ranges from 0.16×10^{-9} to $0.38 \times 10^{-9} \text{ m}^2$, comparable to that of trabecular bones. The stiffness and strength of the designed structures range from 1.08 to 4.47 GPa and 147 to 295 MPa, respectively, reasonably consistent with natural bone. Finally, the study proposes a conceptual design framework that isolates the correlation between the solid fraction of the lattices and the expected biomechanical behavior. Overall, the study highlights the potential of additive manufacturing in creating geometrically complex and mechanically tailored implants for bone tissue reconstruction.

Keywords Patient-specific implant · Additive manufacturing · Selective laser melting (SLM) · Trabecular bone · TPMS structure

1 Introduction

In the field of biomedical applications, titanium and its alloys are widely used due to their unique properties, including excellent mechanical properties such as high specific strength and stiffness, high fracture toughness, great corrosion resistance, and special biocompatibility (Dhiman et al. 2021, 2019; Liu et al. 2020; Shah et al. 2016; Singh et al. 2020; Singla et al. 2021). However, despite these desirable characteristics, one major drawback of titanium implants is

their elastic modulus. The elastic modulus of titanium alloys, particularly Ti6Al4V, is 110 GPa (Geetha et al. 2009), which is higher than the elastic modulus of human bone ranging from 0.5 GPa to a maximum of 30 GPa (Katz 1980; Ma et al. 2019a, b). This modulus mismatch can lead to uneven load distribution at the interface of natural bone and implant, which in turn can cause implant loosening or autogenous bone fracture (Krishna et al. 2007). This phenomenon is referred to as “stress shielding,” which can decrease implant longevity (Aufa et al. 2022). One solution to this problem is the use of “micro-architected” implants with lightweight lattice structures. However, the architecture of these structures plays a critical role, as the geometry, strut size, and solid fraction not only affect the mechanical behavior of the implant but also cell attachment, growth, and nutrient transport (Benedetti et al. 2021; Hsieh et al. 2021; van Blitterswijk et al. 1986). Therefore, the implant's geometry should be tailored to prevent osteonecrosis and osteogenesis deformities around the implant.

✉ Aziz Shafiei-Zarghani
a3shafiei@gmail.com; ashafiei@shirazu.ac.ir

¹ Department of Materials Science and Engineering, School of Materials and Civil Engineering, Shiraz University, Shiraz, Iran

² Department of Medicine and Health, Shiraz3D Technology Center for Digital Manufacturing, Shiraz, Iran

³ Design and Modeling Department, Mehrawin, Shiraz, Iran

In recent years, triply periodic minimal surfaces (TPMS) have garnered attention as a versatile option for micro-architected implants due to their zero-mean curvature and high specific surface area, which create a large surface area for cell growth (Bidan et al. 2013; Jinnai et al. 2002). TPMS structures have unique geometrical features that promote cell growth and attachment, and Bobbert et al. (2017) reported that they also possess relatively high strength with low stiffness. The advantage of TPMS structures lies in their ability to be tailored to mimic the properties of injured bone by controlling their equations and modifying parameters such as channel sizes. Various types of TPMS structures exist, including Schwartz primitive, Schwartz diamond, and gyroid. Each structure has its own unique properties, and it is difficult to determine which structure is superior. However, the gyroid structure has been found to have excellent mechanical properties and interesting self-supported features (Yan et al. 2014). Studies comparing compressive and tensile strength of TPMS structures found that the gyroid structure exhibits the finest mechanical behavior (Yu et al. 2020). Barba et al. (2019) concluded that the choice of lattice topology strongly influences the geometrical precision that can be achieved, and that the gyroid structure presents superior manufacturability and mechanical behavior. Therefore, the gyroid structure was selected for this work. Due to the complex and periodic architecture of TPMS structures, their three-dimensional (3D) production was not possible until the advent of 3D printing. Selective laser melting (SLM) is an additive manufacturing method that uses a powder bed and heat source to create 3D metal shapes with high dimensional accuracy. SLM enables the production of complex scaffolds with excellent quality that was impossible with conventional methods (Bertol et al. 2010; Mullen et al. 2009; Yuan et al. 2019).

In light of the critical nature of producing implants that mimic the mechanical properties of damaged bones, this study aims to explore and evaluate the mechanical properties of various gyroid lattice structures with solid fractions

of 0.16, 0.26, 0.36, and 0.56. Two groups of samples were produced using the Ti6Al4V alloy and SLM machine, respectively, to examine their manufacturability and mass-flow properties while validating the numerical assessments of mechanical behaviors. In essence, the primary objective is to identify a new and straightforward correlation between the solid fraction (relative density) of the internal architecture of implants and their stiffness, strength, and energy absorption properties. The proposed equations offer a swift and practical method for designing trabecular-like structures of customized implants that can be readily employed in clinical settings.

2 Materials and Methods

2.1 Design and Fabrication of Structures

The current investigation involved the conversion of the mathematical equation of the gyroid structure into a 3D computer-aided design (CAD) model, which was achieved using Rhinoceros 7 commercial software in conjunction with the Grasshopper plugin. Subsequently, the Autodesk Netfabb Ultimate 2021 software was utilized to modify and prepare the model for 3D printing. The theoretical equation of the gyroid structure is presented in Eq. (1) below, which was adapted from a review on equations for TPMS geometries by von Schnering and Nesper (1991) and a combination of works presented in the literature (Feng et al. 2019; Yan et al. 2014; Yu et al. 2020; Barba et al. 2019).

$$\cos(ax)\sin(by) + \cos(by)\sin(cz) + \cos(cz)\sin(ax) = 0 \quad (1)$$

Here, the variables a , b , and c determine the solid fraction of the structure, which refers to the relative density of the struts and equals the ratio of the struts' volume to the total volume. These variables also determine the strut and cell size of the structure. Figure 1 illustrates different views of a gyroid

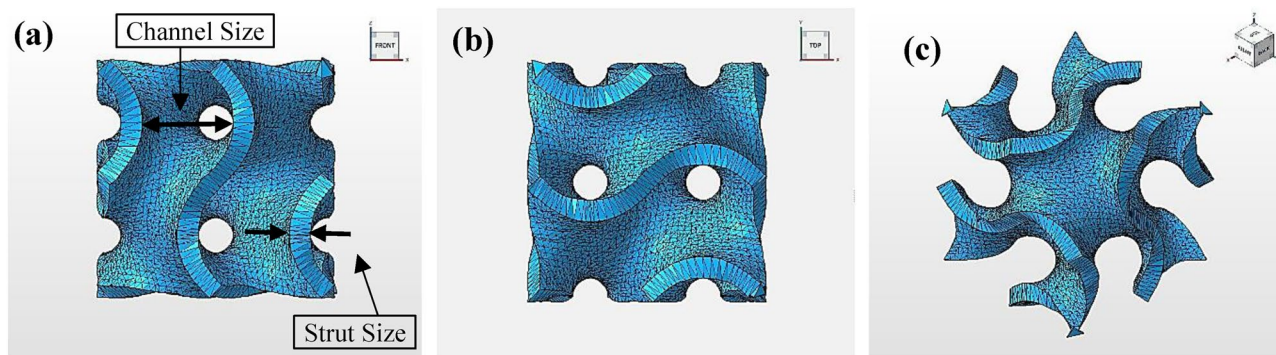


Fig. 1 a Gyroid unit cell architecture in front, b top, and c 3D views

unit cell. The present study involved the design of five different gyroid TPMS structures, each with identical strut sizes of 300 μm and different solid fractions of 0.16, 0.26, 0.36, and 0.56. The dimensions of the designed samples were selected to be 6 \times 6 \times 12 mm based on the ISO13314 standard. As represented in Fig. 2, two groups of samples with solid fractions of 0.26 and 0.56 were manufactured in an argon gas atmosphere by an SLM machine (NOURA M100P) with optimized parameters, maximum laser power of 300 W, and layer thickness of 30 μm . The Ti6Al4V powder used for this fabrication was gas-atomized with a nearly spherical shape and particle size of less than 65 μm . The powder's elemental composition is reported in Table 1. The building direction was in parallel with the Z axis of CAD models, and 400–450 slices formed the final shapes (Fig. 2). At the end of fabrication, all samples were removed from the platform by a wire-cutting machine and ultrasonically cleaned. In order to remove the unsintered powder, post-processing sandblasting was performed on all specimens.

2.2 Measurement and Morphological Characterization

In order to evaluate the manufacturability of designed lattices, a micro-computed tomography (micro-CT, LOTUS in Vivo) was utilized to scan the samples and characterize their 3D morphology. For this purpose, a 10- μm -resolution micro-CT scanner was used at a tube voltage of 90 kV and tube current of 58 μA . Thereafter, 3D models were reconstructed using Avizo Lite 2019 software.

Calculating the percentage of solid and empty parts is a theoretical impossibility without precise knowledge of the structures' densities. As a result, the samples were immersed in alcohol for 2 h, after which their densities were determined using Archimedes' formula. This formula is presented in Eq. (2) (Léon Y León 1998; Yáñez et al. 2018):

$$\rho_s = \left(\frac{\rho_{\text{alc}} * W_a}{W_a - W_{\text{alc}}} \right) \quad (2)$$

where ρ_s is the sample density, W_a and W_{alc} are the weights of the samples in air and alcohol, respectively, and ρ_{alc} is the

Table 1 Chemical composition of Ti6Al4V powder used in this study

Element	Min. wt%	Max. wt%
Al	5.50	6.75
V	3.50	4.50
Fe	–	0.30
O	–	0.20
C	–	0.08
N	–	0.05
H	–	0.015
Y	–	0.005
Other elements each	–	0.10
Other elements total	–	0.40
Ti	Bal	

density of alcohol (0.789 g/cm^3). Following the determination of the density, the relative density (solid fraction) was then calculated using Eq. (3) (Léon Y León 1998; Yáñez et al. 2018), where ρ_d is the theoretical bulk density of Ti6Al4V (4.42 g/cm^3):

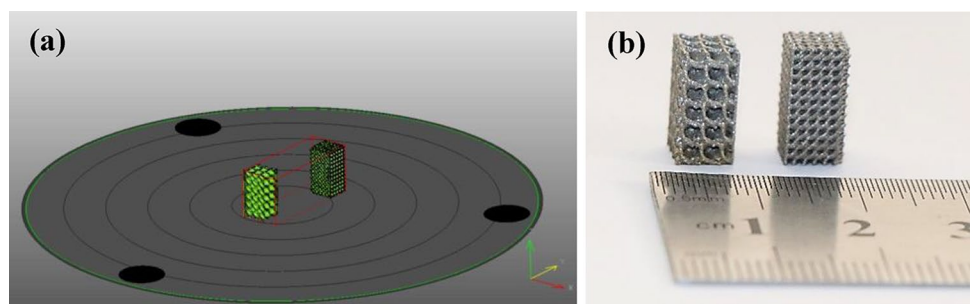
$$P_v = \left(\frac{\rho_s}{\rho_d} \right) \quad (3)$$

The microstructure of the structures was examined using an optical microscope (Dino Eye. AM 423X) and a scanning electron microscope (SEM, VEGA3 TESCAN) for finer details. However, before conducting any microstructure observations, the samples were cut, mounted, grounded by SiC papers (#500, #800, #1000, #1500, and #2000), polished with diamond paste, and etched for 35 s in Kroll etchant solution (100 ml H₂O, 5 ml HNO₃, and 2.5 ml HF).

2.3 Permeability Measurement

To assess the permeability of the samples, the falling-head method was employed, with each structure undergoing three separate measurements to ensure precision of data. Figure 3 illustrates the experimental setup where the sample was affixed to the end of the standpipe, which was then filled with water. The time t_1 and t_2 were recorded at heights L_1

Fig. 2 **a** The building orientation of samples in the manufacturing process, and **b** the manufactured samples



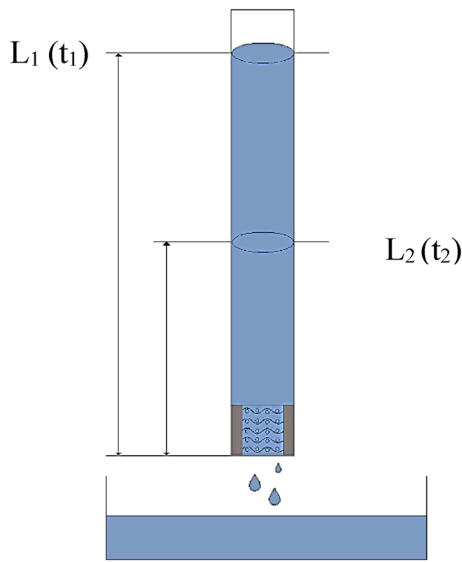


Fig. 3 Schematic of permeability measurement (falling-head method)

and L_2 , respectively, which were constant for all samples. Utilizing Darcy’s law (Eq. 4), the permeability (k) was calculated as follows:

$$k = \frac{K\mu}{\rho g} \tag{4}$$

where μ represents the dynamic viscosity coefficient of water, ρ is the density of water, g is the gravitational constant, and K is the hydraulic conductivity, which is determined by the following formula (Eq. 5):

$$K = \frac{aH}{A(t_2 - t_1)} \ln\left(\frac{L_1}{L_2}\right) \tag{5}$$

Here, H represents the height of the samples, and a and A denote the cross-sectional areas of the standpipe and samples, respectively (Li et al. 2019a, b; Pennella et al. 2013).

2.4 Mechanical Behavior Evaluation

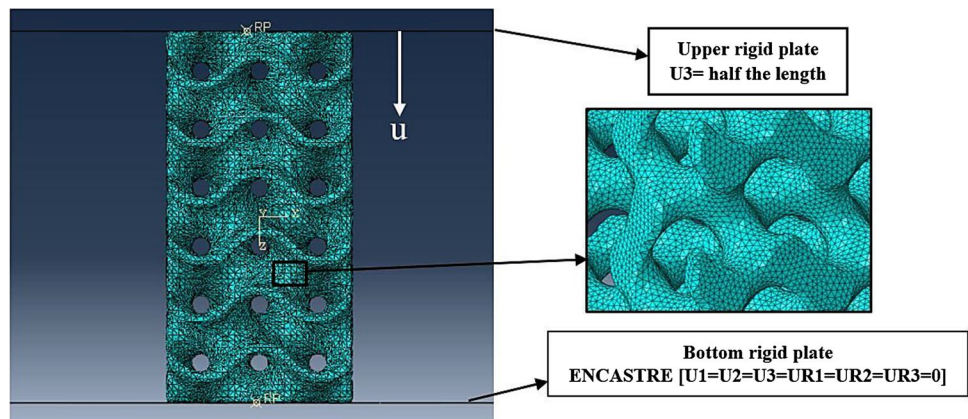
The creation of a finite element model (FEM) for the numerical analysis of designed structures was accomplished using Abaqus/Explicit. The 3D models were positioned between two rigid plates: the lower plate was fixed, and all its degrees of freedom were closed, while the upper plate was movable and loaded along the Z axis at a constant speed. The upper surface of the sample was subjected to a vertical displacement that compressed the specimen to 50% of its length, with half the length of the sample being the applied boundary conditions, as shown in Fig. 4.

For the finite element analysis, isotropic material properties were considered, and since it has been established that the mechanical properties of additively manufactured materials differ from those of conventionally produced materials, the properties of additively manufactured Ti6Al4V alloy were obtained from the literature and inserted into Abaqus. For the elastic properties, an elastic modulus of 107 GPa and a Poisson’s ratio of 0.3 were used (Wang and Li 2018). The plastic deformation of Ti6Al4V is described by the Johnson–Cook plasticity model (Johnson and Cook 1983), which accounts for strain rate, thermal softening, and strain hardening. According to the model, the flow stress in plastic region can be represented by the equation below:

$$\sigma_s = \left[A + B(\epsilon_e)^N \right] \cdot \left[1 + C \ln\left(\frac{\dot{\epsilon}^p}{\dot{\epsilon}^0}\right) \right] \cdot \left[1 - \left(\frac{T - T_{room}}{T_m - T_{room}}\right)^M \right] \tag{6}$$

where A , B , N , C , and M are constant values of material-related parameters according to the flow stress data, and ϵ_e , $\dot{\epsilon}^p$, and $\dot{\epsilon}^0$ are the equivalent plastic strain, equivalent plastic strain rate, and the reference equivalent plastic strain rate, respectively. T_{room} is the room temperature, and T_m is the absolute melting temperature. The input parameters of the Johnson–Cook model for Ti6Al4V were obtained from

Fig. 4 Boundary conditions in simulation



previous studies (Wang and Li 2018; Wauthle et al. 2015), as listed in Table 2.

To bridge the gap between simulated and real behavior, a compression test was performed on two lattice structures having solid fractions of 0.26 and 0.56. The unidirectional compression tests were conducted on these samples at room temperature using a universal testing machine, in accordance with ISO13314 instruction. The test was performed at a constant strain rate of 0.5 mm/min, and the load–displacement curve was recorded. The resulting data was then used to calculate the stress (σ), strain (ϵ), elastic modulus (E), and yield strength (σ_y) for each test. Finally, stress–strain curves were plotted using the obtained data.

Table 2 Constitutive parameters of the Johnson–Cook plasticity model used in the FEM

A (MPa)	B (MPa)	N	C	M
1567	952	0.4	0	0

3 Results and Discussion

3.1 Manufacturability

Figure 5 presents a comparison between the 3D models of primary CAD files and their reconstructed counterparts using micro-CT data, along with their respective cross sections. It is evident that the samples were successfully built with a high degree of dimensional accuracy. Moreover, the SEM images of the samples' top surfaces depicted in Fig. 6 further support this observation. Table 3 tabulates the solid fraction and channel size of the samples obtained from multiple sources, including micro-CT data, density measurements, microscopic observations, and the CAD files. The table shows that the channel sizes of the manufactured samples are slightly smaller than the designed values. Specifically, the strut size increased from 300 μm to approximately 315 μm after the manufacturing process. However, this is a

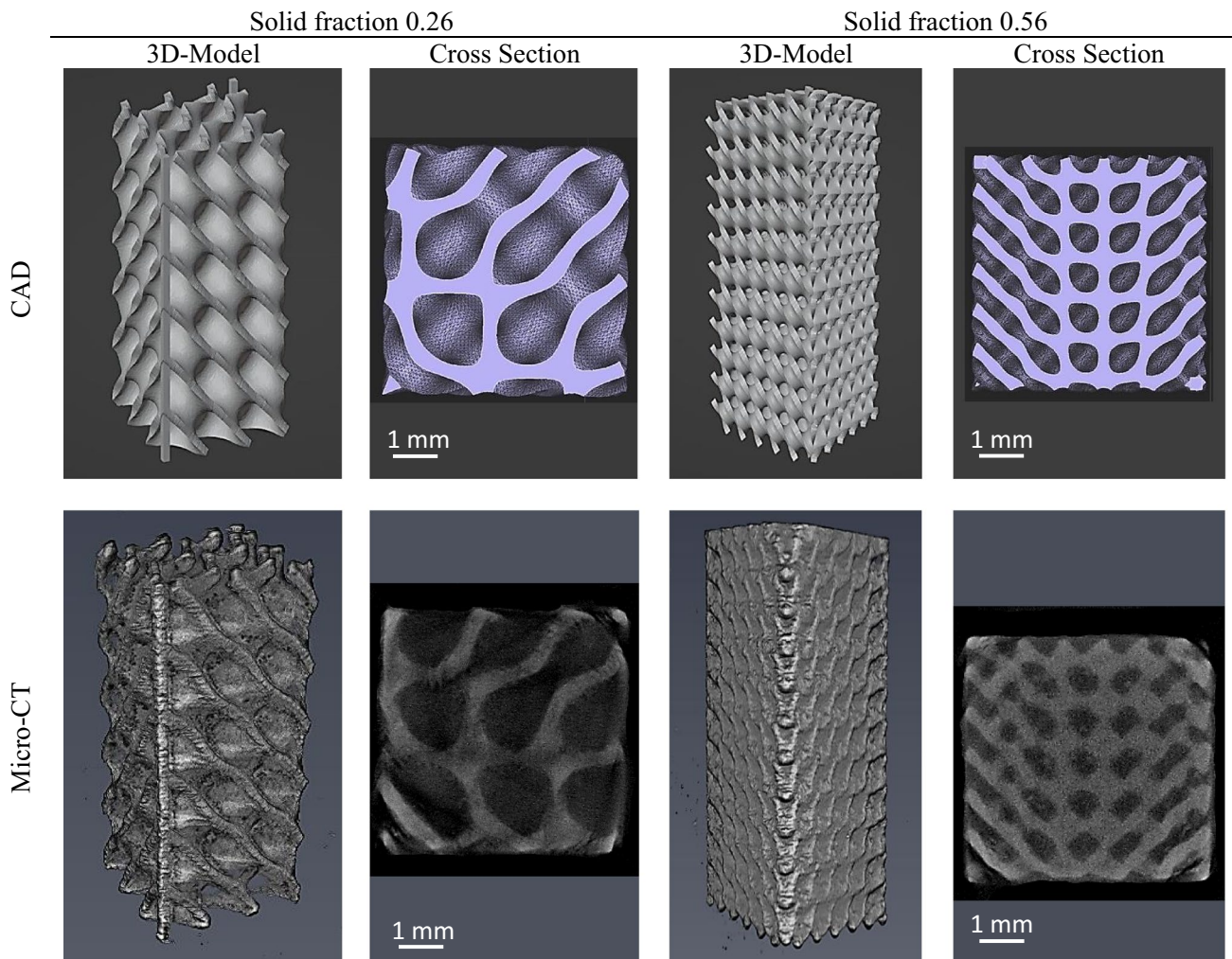


Fig. 5 3D designs and cross section of samples from both CAD and micro-CT data

Fig. 6 SEM images from top surfaces of samples with solid fractions of **a** 0.26 and **b** 0.56

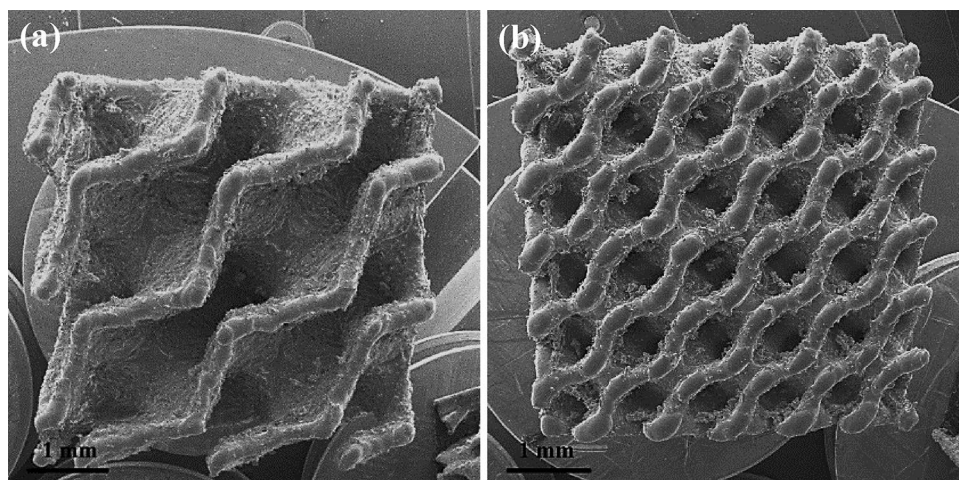


Table 3 Geometrical data obtained from the design and the computation

Solid fraction, %			Channel size, μm		
Designed	Micro-CT	Density measurements	Designed	Micro-CT	Microscopic observations
26	29	31	1600	1510	1530
56	56	58	600	550	560

known outcome of the SLM process, where the thermocapillary flow results in unstable molten pools, leading to a relatively small difference in strut size that can be ignored (Gu et al. 2013; Lee et al. 1998; Ma et al. 2019b; Rombouts et al. 2006; Yadroitsev et al. 2007). This also explains the higher solid fraction observed after the construction of the samples.

Microstructural characterization of the samples (Fig. 7) revealed that both groups exhibit the same type of microstructure, namely the α' phase, which comprises fine and orthogonally oriented martensitic laths. The formation of

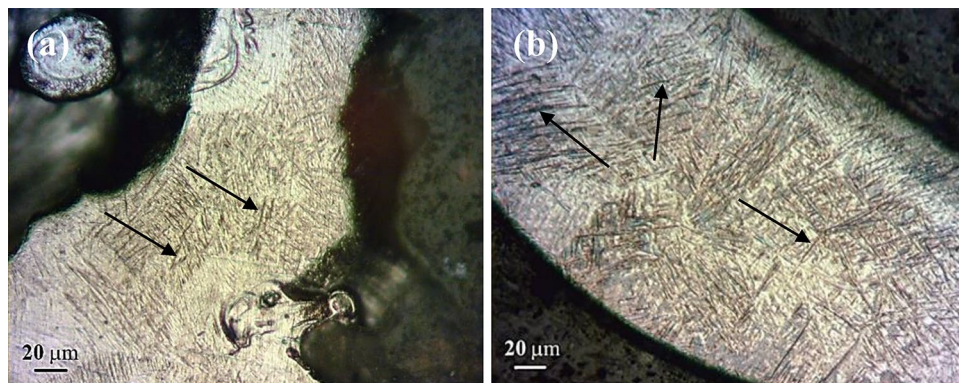
this phase is a consequence of the rapid cooling rate during the SLM process, as many of the previous β transforms into the acicular α' martensitic phase (Eshawish et al. 2021; Fotovvati et al. 2012).

3.2 Permeability

Permeability is a crucial parameter for analyzing the mass transport characteristics of lattice structures, as they can significantly impact bone growth (Hollister 2005; Sanz-Herrera et al. 2008; Jones et al. 2009; Mitsak et al. 2011). Quantitatively, permeability measures the ability of a porous structure to conduct fluid flow, which is influenced by a combination of interconnectivity, solid fraction, channel size, orientation, and tortuosity. It is important to note that inadequate permeability values may lead to the formation of cartilaginous instead of bone tissue, while higher values have been shown to enhance bone ingrowth (Kempainen 2008; Jeong et al. 2011; Mitsak et al. 2011).

The values of permeability in trabecular bone depend on different factors, such as the anatomic site and age of the person. For instance, Nauman and colleagues (1999) reported that the permeability of the proximal femur is significantly

Fig. 7 Optical microscopy (OM) images from etched surfaces of samples with solid fractions of **a** 0.26 and **b** 0.56. Typical acicular martensitic α' phases are indicated by arrows



greater than that of the vertebral body. Hence, a range of permeabilities is found in the literature (1.00×10^{-11} to $1.21 \times 10^{-8} \text{ m}^2$), rather than a specific value. In the present study, the permeabilities of samples with solid fractions of 0.26 and 0.56 were found to be 0.16×10^{-9} and $0.38 \times 10^{-9} \text{ m}^2$, respectively. In both cases, the values are applicable, and as evident, the higher permeability of the 0.26 solid fraction is due to its larger channel size. A straight-through connecting structure would result in a higher permeability, and the obstructive structure of the gyroid against the fluid flow is the reason why the permeabilities of structures in this study are not in the higher-value part of the abovementioned range.

3.3 Mechanical Properties

3.3.1 Compression Behavior

The stress–strain behavior of the structures under investigation is graphically depicted in Fig. 8. The initial linear region represents the elastic behavior, where the slope of the curve reflects the stiffness or elastic modulus of each structure. At the end of this zone, the highest peak on the curve signifies the maximum stress and strength the structures can withstand. Subsequently, the curves enter the plastic region, where even with a slight increase in stress, a wide range of strain and deformation can be observed, making them suitable for high-energy absorption applications (Zhang et al. 2021). For solid fractions of 0.36 and 0.56, the last portion of the curves, where the stress increases after the plateau region, is referred to as densification. This increase in stress is due to the struts of the structures coming into contact with each other. However, samples with lower solid fractions did not experience this phenomenon. Figure 9 illustrates the displacement and von Mises stress distributions of samples at different strains, highlighting the densification of the structures.

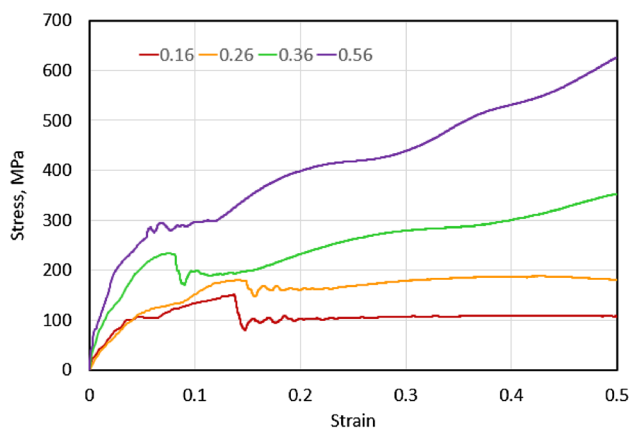


Fig. 8 Stress–strain curves from finite element analysis for different solid fractions

The stress–strain curves obtained from the uniaxial compression tests of manufactured structures are depicted in Fig. 10, along with images of the compressed samples. These curves exhibit good stability and follow a similar trend to those obtained from the finite element analysis. The fluctuations observed in the plateau region indicate that the structure fails layer by layer. Table 4 provides the results of the experiments, in addition to the finite element analysis results. Consistent with the finite element analysis findings, the sample with a solid fraction of 0.56 displays a higher yield strength and stiffness in the compression test. An increase in the solid fraction leads to a corresponding increase in the stiffness and yield strength of the structures. Designing the implant in a way that its stiffness is within the appropriate range (1.30–5.3 GPa for tibia, femur, and proximal bone; Gibson and Ashby 2014) can prevent the stress shielding phenomena. As the table demonstrates, the elastic modulus of structures in this research is also within this range. Discrepancies between the experimental and numerical values can be attributed to factors such as discrepancies between the fabricated lattice geometry and the nominal CAD input, manufacturing imperfections, unmelted powders, and surface abnormalities (Wauthle et al. 2015; Dallago et al. 2018). Nonetheless, a discrepancy of less than 10% between the experimental and finite element analysis results is considered acceptable, which is in line with the literature (Dallago et al. 2018).

3.3.2 Mechanical Properties and Solid Fraction Relations

The correlation between mechanical properties of lattice structures and their solid fraction (or relative density) can be described by the exponential function proposed by Gibson and Ashby (2014), which is shown below:

$$E^* = C_1 \rho^n + E_0 \quad (7)$$

$$\sigma^* = C_2 \rho^m + \sigma_0 \quad (8)$$

where ρ is the solid fraction or relative density of the structure, E_0 and σ_0 are the offset of the elastic modulus and yield strength, respectively, and C_1 , C_2 , n and m are the material and structural constants. By plotting the changes in the mechanical properties of structures based on their solid fractions on a logarithmic scale, the constants of Eqs. (7) and (8) can be determined (Fig. 11). These equations can be utilized to simplify the process of customized implant design. Based on the required strength and stiffness (determined by factors such as age, gender, bone density, etc.), the safe and appropriate solid fraction range of the implant can be selected using the derived equations. This method can greatly facilitate the development of personalized and customized implants.

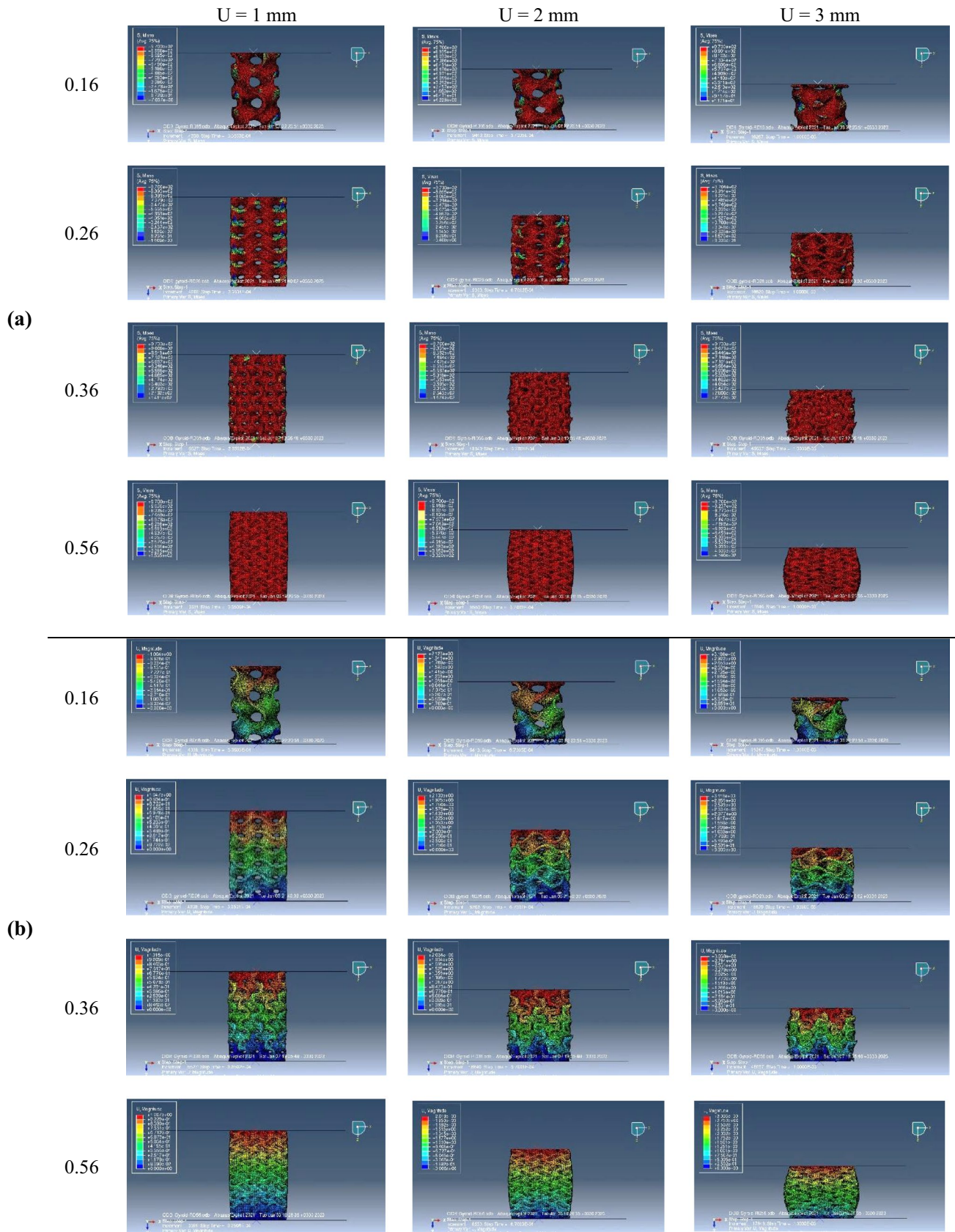


Fig. 9 Compressive deformation at different compressive strains: a) von Mises stress and b) displacement distributions

Fig. 10 Stress–strain curves from the compression test and compressed samples

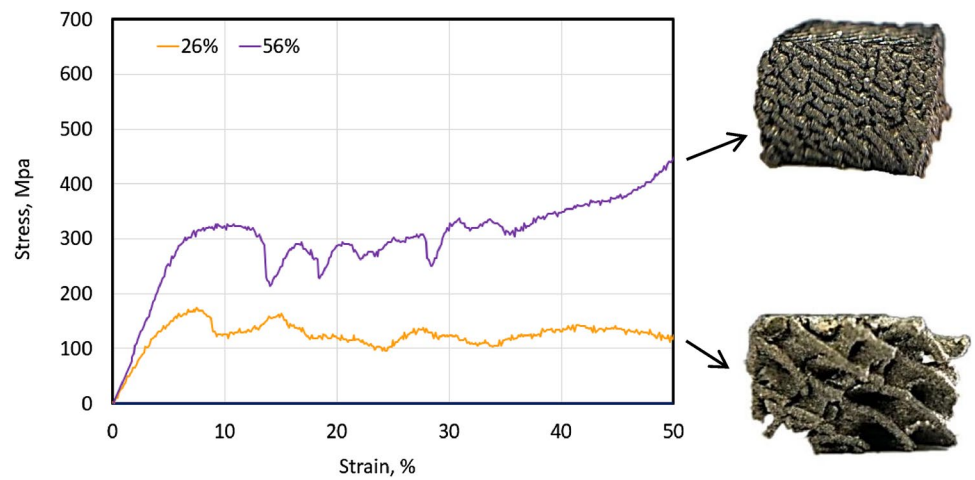


Table 4 The effect of relative density on the mechanical properties of structures

Solid fraction	Stiffness, GPa			Yield strength, MPa		
	Experiment	Simulation	% error	Experiment	Simulation	% error
0.16	–	1.08	–	–	147.02	–
0.26	2.41	2.23	–7.1	171.42	168.78	–1.5
0.36	–	3.07	–	–	232.24	–
0.56	4.63	4.47	–2.1	305.17	295.13	–3.3

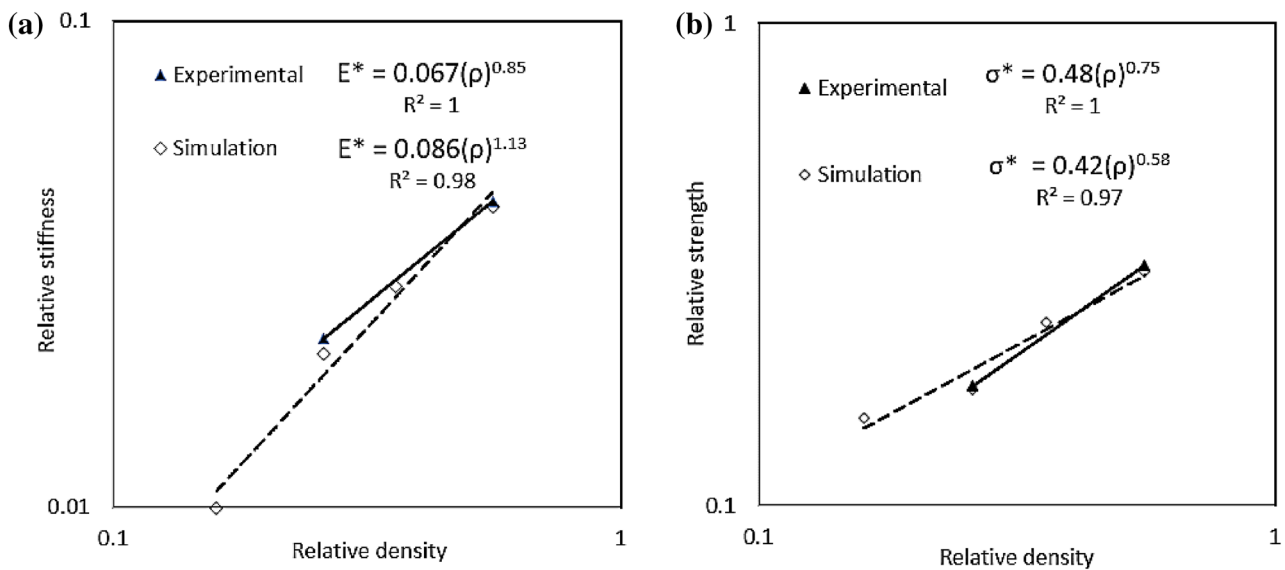


Fig. 11 Relationship between **a** relative stiffness, and **b** relative strength and relative density for implant design

3.3.3 Energy Absorption Evaluation

The energy absorption capacity is a determining characteristic of lattice structures to evaluate their mechanical properties. The solid fraction or relative density is one of the most influencing parameters of cellular structures, and

therefore, understanding the relationship between relative density and energy absorption properties is of great importance. The energy absorption of the structures during the compression test can be calculated as below by integrating the stress–strain curve (Li et al. 2019a, b; Ma et al. 2021; Zhang et al. 2021):

$$W = \int_0^{\varepsilon_d} \sigma(\varepsilon) d\varepsilon \quad (9)$$

where ε_d is the maximum strain at the onset of the densification stage. The densification strain (ε_d) is defined as the corresponding strain to the maximum energy absorption efficiency $\eta(\varepsilon)$, which can be written as follows (Li et al. 2006):

$$\eta(\varepsilon) = \frac{\int_0^{\varepsilon} \sigma(\varepsilon) d\varepsilon}{\sigma(\varepsilon)}, \quad \frac{d\eta(\varepsilon)}{d\varepsilon} \Big|_{\varepsilon=\varepsilon_d} = 0 \quad (10)$$

where $\sigma(\varepsilon)$ is the peak stress during the deformation up to the strain ε . In effect, the densification strain refers to the corresponding strain to the peak point of the energy absorption efficiency curve. Specific energy absorption (SEA), which is shown in Eq. 11, is the most common method used to reveal the energy absorption capability (Li et al. 2019a, b; Ma et al. 2021; Zhang et al. 2021):

$$SEA = \frac{\int_0^{\varepsilon_d} \sigma(\varepsilon) d\varepsilon}{\rho} \quad (11)$$

where ρ is the relative density of the structure. The relationship between the energy absorption and the specific energy absorption values of lattice structures, as well as strain values for different solid fractions, is presented in Fig. 12. Furthermore, the energy absorption efficacy of the samples obtained from both experimental and numerical methods is listed in Table 5, revealing an increase in energy absorption capacity with the increase of relative density. Notably, the results obtained from both methods indicate an acceptable similarity. Although the energy absorption capacity of the designed structures is observed to increase with solid fraction, the specific energy absorption of the samples falls

Table 5 Energy absorption efficacy values obtained from compression tests and FEM

Solid fraction, %	Energy absorption efficacy, %		
	Experiment	Simulation	% error
16	–	72.38	–
26	76.46	80.44	5.2
36	–	64.67	–
56	58.19	54.12	–7

within a similar range, suggesting that the samples possess analogous energy absorption properties due to their comparable structures. However, upon calculating energy absorption efficacy values from experimental and finite element method (FEM) results, it is evident that the samples with a solid fraction of 0.26 exhibit the highest values. This can be attributed to the compression behavior of this sample, which exhibits a stress–strain curve with fewer fluctuations. The smoother stress–strain curve, combined with the higher densification strain in samples with lower solid fractions, enables them to absorb more energy at the same stress. Moreover, it is observed that as the solid fraction increases from 0.26 to 0.56 mm, the energy absorption efficiency of the structures is considerably reduced by approximately 26%. This decline is attributed to the higher densification strain of the sample with a solid fraction of 0.56. In conclusion, the energy absorption capacity of structures increases with an increase in solid fraction. Additionally, while all structures display relatively similar energy absorption behavior, structures with lower solid fractions exhibit higher values of energy absorption efficacy.

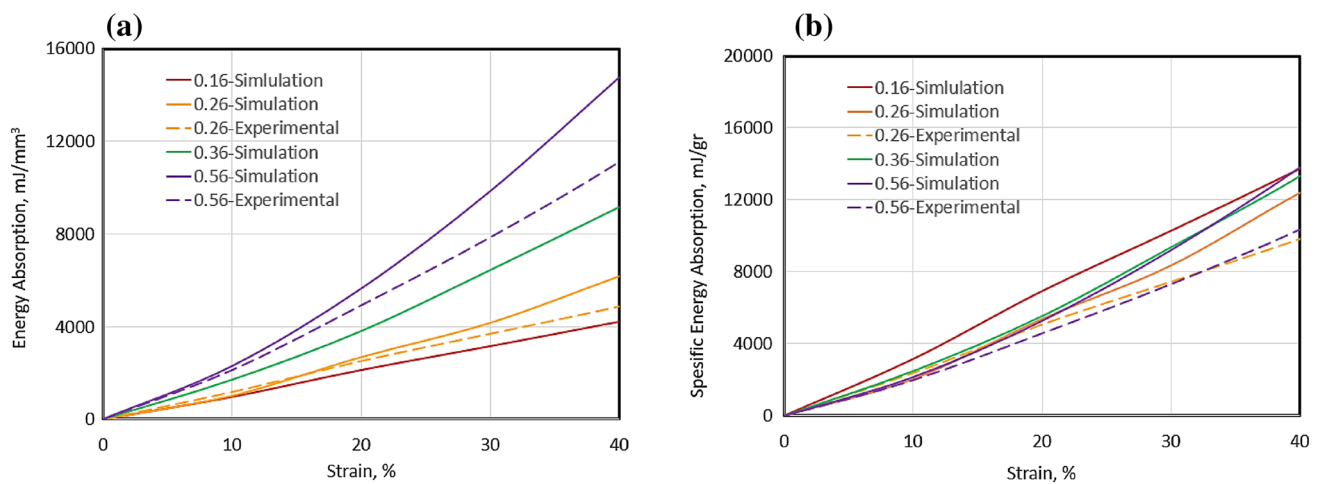


Fig. 12 a Energy absorption and b specific energy absorption of the structures versus strain

4 Conclusions

This study aimed to establish a clear correlation between the solid fraction of the gyroid lattice structure and its mechanical properties, such as stiffness, strength, and energy absorption. This information is critical for the development of custom trabecular bone implants. Specifically, the study focused on the tibia component of knee joint replacements. To investigate the relationship between the solid fraction and mechanical properties, gyroid structures with solid fractions of 16%, 26%, 36%, and 56% were designed and analyzed using finite element analysis. To validate the simulation results and evaluate the manufacturability and permeability of the structures, two of the structures with solid fractions of 26% and 56% were fabricated using the SLM technique. The key findings of the study are presented below.

- 1- Ti6Al4V lattices with gyroid structures were produced using selective laser melting (SLM) and exhibited stable manufacturability. The accuracy of the solid fractions and the manufacturing deviation of the struts and channels size confirmed the stability of the manufacturing process.
- 2- The permeability behavior of the gyroid structures was evaluated through an experimental method. The permeability of the samples ranged from 0.16×10^{-9} to $0.38 \times 10^{-9} \text{ m}^2$, similar to the permeability range of the tibia bone. Furthermore, the permeabilities decreased as the solid fraction increased. However, the straight-through connecting structure of the gyroid structure exhibited an obstructive behavior against fluid flow.
- 3- FEM and experimental assessment of the compression behavior of the Ti6Al4V gyroid lattices produced by SLM revealed that the structures have adjustable mechanical properties. The structures can reduce implant stiffness to the same range as trabecular bone stiffness. The stiffness and yield strengths of the gyroid lattices ranged from 1.08 to 4.47 GPa and 147 to 295 MPa, respectively, satisfying the requirements of natural trabecular bones. The designed structures can match the stiffness of human bone by altering the solid fraction, thereby reducing the probability of stress shielding phenomenon and implant failure. Additionally, their high mechanical strength prevents implant failure under mechanical loading.
- 4- The mechanical behavior assessment of Ti6Al4V gyroid lattices fabricated using SLM showed that the solid fraction of the structure plays a crucial role in determining its strength and stiffness. These relationships can be utilized to select the optimal solid fraction of the structure for implant design, taking into account the patient's age

and bone density. By doing so, personalized implant design can be simplified and accelerated.

- 5- Increasing the solid fraction of the gyroid structure leads to improved energy absorption capability. However, specific energy absorption values were relatively similar across all structures due to their identical lattice structure. Among the structures evaluated, the gyroid lattice with 26% solid fraction exhibited the highest energy absorption efficacy due to its smoother stress–strain curve and high densification strain. The results demonstrated that gyroid lattices with lower solid fractions are capable of absorbing more energy at the same stress compared to those with higher solid fractions.

Acknowledgements This work was supported by the Shiraz University and Mehrawin Company. The micro-computed tomography (micro-CT) test machine used in this study was funded by the preclinical laboratory of Tehran University of Medical Sciences.

Funding This work was supported by the Shiraz University and the Mehrawin Co.

Declarations

Conflict of interest The authors report there are no competing interests to declare.

References

- Aufa AN, Hassan MZ, Ismail Z (2022) Recent advances in Ti-6Al-4V additively manufactured by selective laser melting for biomedical implants: prospect development. *J Alloys Compd* 896:163072. <https://doi.org/10.1016/J.JALLCOM.2021.163072>
- Barba D, Alabort E, Reed RC (2019) Synthetic bone: Design by additive manufacturing. *Acta Biomater* 97:637–656. <https://doi.org/10.1016/J.ACTBIO.2019.07.049>
- Benedetti M, du Plessis A, Ritchie RO, Dallago M, Razavi SMJ, Berto F (2021) Architected cellular materials: A review on their mechanical properties towards fatigue-tolerant design and fabrication. *Mater Sci Eng R Rep* 144:100606. <https://doi.org/10.1016/J.MSER.2021.100606>
- Bertol LS, Júnior WK, da Silva FP, Aumund-Kopp C (2010) Medical design: direct metal laser sintering of Ti–6Al–4V. *Mater Des* 31:3982–3988. <https://doi.org/10.1016/J.MATDES.2010.02.050>
- Bidan CM, Wang FM, Dunlop JWC (2013) A three-dimensional model for tissue deposition on complex surfaces. *Comput Methods Biomech Biomed Eng* 16:1056–1070. <https://doi.org/10.1080/10255842.2013.774384>
- Bobbert FSL, Lietaert K, Eftekhari AA, Poursan B, Ahmadi SM, Weinsans H, Zadpoor AA (2017) Additively manufactured metallic porous biomaterials based on minimal surfaces: a unique combination of topological, mechanical, and mass transport properties. *Acta Biomater* 53:572–584. <https://doi.org/10.1016/J.ACTBIO.2017.02.024>
- Dallago M, Fontanari V, Torresani E, Leoni M, Pederzolini C, Potrich C, Benedetti M (2018) Fatigue and biological properties of Ti-6Al-4V ELI cellular structures with variously arranged cubic cells made by selective laser melting. *J Mech Behav Biomed Mater* 78:381–394. <https://doi.org/10.1016/j.jmbbm.2017.11.044>

- Dhiman S, Sidhu SS, Bains PS, Bahraminasab M (2019) Mechanobiological assessment of Ti-6Al-4V fabricated via selective laser melting technique: a review. *Rapid Prototyp J* 25:1266–1284. <https://doi.org/10.1108/RPJ-03-2019-0057/FULL/XML>
- Dhiman S, Joshi RS, Singh S, Gill SS, Singh H, Kumar R, Kumar V (2021) A framework for effective and clean conversion of machining waste into metal powder feedstock for additive manufacturing. *Clean Eng Technol* 4:100151. <https://doi.org/10.1016/J.CLET.2021.100151>
- Eshawish N, Malinov S, Sha W, Walls P (2021) Microstructure and mechanical properties of Ti-6Al-4V manufactured by selective laser melting after stress relieving, hot isostatic pressing treatment, and post-heat treatment. *J Mater Eng Perform* 30:5290–5296. <https://doi.org/10.1007/S11665-021-05753-W>
- Feng J, Fu J, Lin Z, Shang C, Niu X (2019) Layered infill area generation from triply periodic minimal surfaces for additive manufacturing. *CAD Comput Aided Des* 107:50–63. <https://doi.org/10.1016/j.cad.2018.09.005>
- Fotovvati B, Namdari N, Dehghanghadikolaei A, Dai N, Zhang J, Chen Y, al Liu W, Liu Z, Simonelli M, Tse YY, Tuck C (2012) Microstructure of Ti-6Al-4V produced by selective laser melting. *J Phys Conf Ser* 371:012084. <https://doi.org/10.1088/1742-6596/371/1/012084>
- Geetha M, Singh AK, Asokamani R, Gogia AK (2009) Ti based biomaterials, the ultimate choice for orthopaedic implants—a review. *Prog Mater Sci* 54:397–425. <https://doi.org/10.1016/J.PMATSCI.2008.06.004>
- Gibson LJ, Ashby MF (2014) Cellular solids: structure and properties, 2nd edition, Cambridge University Press, pp. 1–510. <https://doi.org/10.1017/CBO9781139878326>
- Gu DD, Meiners W, Wissenbach K, Poprawe R (2013) Laser additive manufacturing of metallic components: materials, processes and mechanisms. *Int Mater Rev* 57:133–164. <https://doi.org/10.1179/1743280411Y.0000000014>
- Hollister SJ (2005) Porous scaffold design for tissue engineering. *Nat Mater* 4(7):518–524. <https://doi.org/10.1038/nmat1421>
- Hsieh MT, Begley MR, Valdevit L (2021) Architected implant designs for long bones: Advantages of minimal surface-based topologies. *Mater Des* 207:109838. <https://doi.org/10.1016/J.MATDES.2021.109838>
- Jeong CG, Zhang H, Hollister SJ (2011) Three-dimensional poly(1,8-octanediol-co-citrate) scaffold pore shape and permeability effects on sub-cutaneous in vivo chondrogenesis using primary chondrocytes. *Acta Biomater* 7(2):505–514. <https://doi.org/10.1016/j.actbio.2010.08.027>
- Jinnai H, Watashiba H, Kajihara T, Nishikawa Y, Takahashi M, Ito M (2002) Surface curvatures of trabecular bone microarchitecture. *Bone* 30:191–194. [https://doi.org/10.1016/S8756-3282\(01\)00672-X](https://doi.org/10.1016/S8756-3282(01)00672-X)
- Johnson GR, Cook WH (1983) A computational constitutive model and data for metals subjected to large strain, high strain rates and high pressures. In: *The seventh international symposium on ballistics*, pp. 541–547.
- Jones AC, Arns CH, Hutmacher DW, Milthorpe BK, Sheppard AP, Knackstedt MA (2009) The correlation of pore morphology, interconnectivity and physical properties of 3D ceramic scaffolds with bone ingrowth. *Biomaterials* 30(7):1440–1451. <https://doi.org/10.1016/j.biomaterials.2008.10.056>
- Katz JL (1980) Anisotropy of Young's modulus of bone. *Nature* 283(5742):106–107. <https://doi.org/10.1038/283106a0>
- Kempainen J (2008) Mechanically stable solid freeform fabricated scaffolds with permeability optimized for cartilage tissue engineering, p. 177. <http://proquest.umi.com.proxy.lib.umich.edu/pqdweb?did=1663913111&Fmt=7&clientId=17822&RQT=309&VName=PQD>
- Krishna BV, Bose S, Bandyopadhyay A (2007) Low stiffness porous Ti structures for load-bearing implants. *Acta Biomater* 3:997–1006. <https://doi.org/10.1016/J.ACTBIO.2007.03.008>
- Lee PD, Quedstedt PN, McLean M (1998) Modelling of Marangoni effects in electron beam melting. *Philos Trans R Soc A Math Phys Eng Sci* 356:1027–1043. <https://doi.org/10.1098/RSTA.1998.0207>
- LéonLeón YCA (1998) New perspectives in mercury porosimetry. *Adv Coll Interface Sci* 76–77:341–372. [https://doi.org/10.1016/S0001-8686\(98\)00052-9](https://doi.org/10.1016/S0001-8686(98)00052-9)
- Li QM, Magkiriadis I, Harrigan JJ (2006) Compressive strain at the onset of densification of cellular solids. *J Cell Plast* 42(5):371–392. <https://doi.org/10.1177/0021955X06063519>
- Li D, Liao W, Dai N, Xie YM (2019) Comparison of mechanical properties and energy absorption of sheet-based and strut-based gyroid cellular structures with graded densities. *Materials*. <https://doi.org/10.3390/MA12132183>
- Li Y, Jahr H, Pavanram P, Bobbert FSL, Puggi U, Zhang XY, Pouran B, Leeftang MA, Weinans H, Zhou J, Zadpoor AA (2019b) Additively manufactured functionally graded biodegradable porous iron. *Acta Biomater* 96:646–661. <https://doi.org/10.1016/J.ACT-BIO.2019.07.013>
- Liu F, Ran Q, Zhao M, Zhang T, Zhang DZ, Su Z (2020) Additively manufactured continuous cell-size gradient porous scaffolds: pore characteristics, mechanical properties and biological responses in vitro. *Materials* (Basel, Switzerland). <https://doi.org/10.3390/MA13112589>
- Ma S, Tang Q, Song J, Han X, Guo F (2019a) Mechanical behaviours and mass transport properties of bone-mimicking scaffolds consisted of Gyroid structures manufactured using selective laser melting. *J Mech Behav Biomed Mater* 93:158–169. <https://doi.org/10.1016/J.JMBBM.2019.01.023>
- Ma X, Zhang DZ, Zhao M, Jiang J, Luo F, Zhou H (2021) Mechanical and energy absorption properties of functionally graded lattice structures based on minimal curved surfaces. *Int J Adv Manuf Technol* 118:995–1008. <https://doi.org/10.1007/S00170-021-07768-Y>
- Mitsak AG, Kempainen JM, Harris MT, Hollister SJ (2011) Effect of polycaprolactone scaffold permeability on bone regeneration in vivo. *Tissue Eng Part A* 17(13–14):1831–1839. <https://doi.org/10.1089/ten.tea.2010.0560>
- Mullen L, Stamp RC, Brooks WK, Jones E, Sutcliffe CJ (2009) Selective Laser Melting: a regular unit cell approach for the manufacture of porous, titanium, bone in-growth constructs, suitable for orthopedic applications. *J Biomed Mater Res Part B Appl Biomater* 89:325–334. <https://doi.org/10.1002/JBM.B.31219>
- Nauman EA, Fong KE, Keaveny TM (1999) Dependence of intertrabecular permeability on flow direction and anatomic site. *Ann Biomed Eng* 27(4):517–524. <https://doi.org/10.1114/1.195>
- Pennella F, Cerino G, Massai D, Gallo D, Falvo D'Urso Labate G, Schiavi A, Deriu MA, Audenino A, Morbiducci U (2013) A survey of methods for the evaluation of tissue engineering scaffold permeability. *Ann Biomed Eng* 41:2027–2041. <https://doi.org/10.1007/S10439-013-0815-5>
- Rombouts M, Kruth JP, Froyen L, Mercelis P (2006) Fundamentals of selective laser melting of alloyed steel powders. *CIRP Ann Manuf Technol* 55:187–192. [https://doi.org/10.1016/S0007-8506\(07\)60395-3](https://doi.org/10.1016/S0007-8506(07)60395-3)
- Sanz-Herrera JA, Garcia-Aznar JM, Doblare M (2008) A mathematical model for bone tissue regeneration inside a specific type of scaffold. *Biomech Model Mechanobiol* 7(5):355–366. <https://doi.org/10.1007/s10237-007-0089-7>
- Shah FA, Trobos M, Thomsen P, Palmquist A (2016) Commercially pure titanium (cp-Ti) versus titanium alloy (Ti6Al4V) materials as bone anchored implants—is one truly better than the other? *Mater Sci Eng C* 62:960–966. <https://doi.org/10.1016/J.MSEC.2016.01.032>

- Singh M, Dhiman S, Singh H, Berndt CC (2020) Optimization of modulation-assisted drilling of Ti-6Al-4V aerospace alloy via response surface method. *Mater Manuf Process* 35:1313–1329. <https://doi.org/10.1080/10426914.2020.1772487>
- Singla AK, Banerjee M, Sharma A, Singh J, Bansal A, Gupta MK, Khanna N, Shahi AS, Goyal DK (2021) Selective laser melting of Ti6Al4V alloy: process parameters, defects and post-treatments. *J Manuf Process* 64:161–187. <https://doi.org/10.1016/J.JMAPRO.2021.01.009>
- The relationship between stress shielding and bone resorption around total hip stems and the effects of flexible materials - PubMed [WWW Document], n.d. URL <https://pubmed.ncbi.nlm.nih.gov/1728998/>. Accessed 24 Sept 2022
- Titanium as the material of choice for cementless femoral components in total hip arthroplasty - PubMed [WWW Document], n.d. URL <https://pubmed.ncbi.nlm.nih.gov/7634595/>. Accessed 13 Nov 2022
- van Blitterswijk CA, Grote JJ, Kuijpers W, Daems WT, de Groot K (1986) Macropore tissue ingrowth: a quantitative and qualitative study on hydroxyapatite ceramic. *Biomaterials* 7:137–143. [https://doi.org/10.1016/0142-9612\(86\)90071-2](https://doi.org/10.1016/0142-9612(86)90071-2)
- von Schnering HG, Nesper R (1991) Nodal surfaces of Fourier series: fundamental invariants of structured matter. *Zeitschrift für Physik B Condensed Matter* 83(3):407–412. <https://doi.org/10.1007/BF01313411>
- Wang Z, Li P (2018) Characterisation and constitutive model of tensile properties of selective laser melted Ti-6Al-4V struts for microlattice structures. *Mater Sci Eng A* 725:350–358. <https://doi.org/10.1016/j.msea.2018.04.006>
- Wauthle R, Vrancken B, Beynaerts B, Jorissen K, Schrooten J, Kruth JP, Van Humbeeck J (2015) Effects of build orientation and heat treatment on the microstructure and mechanical properties of selective laser melted Ti6Al4V lattice structures. *Addit Manuf* 5:77–84. <https://doi.org/10.1016/j.addma.2014.12.008>
- Yadroitsev I, Bertrand P, Smurov I (2007) Parametric analysis of the selective laser melting process. *Appl Surf Sci* 253:8064–8069. <https://doi.org/10.1016/J.APSUSC.2007.02.088>
- Yan C, Hao L, Hussein A, Young P, Raymont D (2014) Advanced light-weight 316L stainless steel cellular lattice structures fabricated via selective laser melting. *Mater Des* 55:533–541. <https://doi.org/10.1016/J.MATDES.2013.10.027>
- Yáñez A, Cuadrado A, Martel O, Afonso H, Monopoli D (2018) Gyroid porous titanium structures: a versatile solution to be used as scaffolds in bone defect reconstruction. *Mater Des* 140:21–29. <https://doi.org/10.1016/j.matdes.2017.11.050>
- Yu G, Li Z, Li S, Zhang Q, Hua Y, Liu H, Zhao X, Dhaidhai DT, Li W, Wang X (2020) The select of internal architecture for porous Ti alloy scaffold: a compromise between mechanical properties and permeability. *Mater Des* 192:108754. <https://doi.org/10.1016/J.MATDES.2020.108754>
- Yuan L, Ding S, Wen C (2019) Additive manufacturing technology for porous metal implant applications and triple minimal surface structures: a review. *Bioact Mater* 4:56–70. <https://doi.org/10.1016/J.BIOACTMAT.2018.12.003>
- Zhang XC, Liu NN, An CC, Wu HX, Li N, Hao KM (2021) Dynamic crushing behaviors and enhanced energy absorption of bio-inspired hierarchical honeycombs with different topologies. *Def Technol*. <https://doi.org/10.1016/J.DT.2021.11.013>

Springer Nature or its licensor (e.g. a society or other partner) holds exclusive rights to this article under a publishing agreement with the author(s) or other rightsholder(s); author self-archiving of the accepted manuscript version of this article is solely governed by the terms of such publishing agreement and applicable law.